



## Spinel $\text{NiCo}_2\text{O}_4$ for use as a high-performance supercapacitor electrode material: Understanding of its electrochemical properties



Yirong Zhu <sup>a</sup>, Xiaobo Ji <sup>a,\*</sup>, Zhengping Wu <sup>a</sup>, Weixin Song <sup>a</sup>, Hongshuai Hou <sup>a</sup>, Zhibin Wu <sup>a</sup>, Xiao He <sup>b</sup>, Qiyuan Chen <sup>a</sup>, Craig E. Banks <sup>c</sup>

<sup>a</sup> Key Laboratory of Resources Chemistry of Nonferrous Metals, Ministry of Education, College of Chemistry and Chemical Engineering, Central South University, Changsha 410083, China

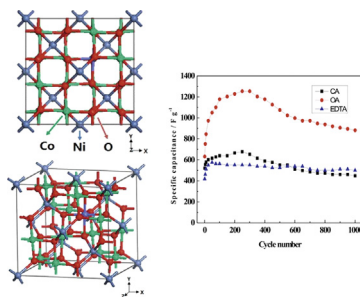
<sup>b</sup> Shenzhen Key Laboratory of Advanced Materials, Department of Materials Science and Engineering, Shenzhen Graduate School, Harbin Institute of Technology, Shenzhen 518055, China

<sup>c</sup> Faculty of Science and Engineering, School of Science and the Environment, Division of Chemistry and Environmental Science, Manchester Metropolitan University, Chester Street, Manchester M1 5GD, Lancs, UK

### HIGHLIGHTS

- Spinel  $\text{NiCo}_2\text{O}_4$  was prepared by sol–gel method using three chelating agents.
- The effect of different chelating agents on the electrochemical properties of the  $\text{NiCo}_2\text{O}_4$  was firstly investigated.
- The first-principles were used for calculation.
- High specific capacitance of  $1254 \text{ F g}^{-1}$  at  $2 \text{ A g}^{-1}$  was obtained using oxalic acid as chelating agent.

### GRAPHICAL ABSTRACT



### ARTICLE INFO

#### Article history:

Received 5 April 2014

Received in revised form

13 May 2014

Accepted 23 May 2014

Available online 5 June 2014

#### Keywords:

Spinel nickel cobaltite

Sol–gel method

Chelating agent

Electrochemical property

Supercapacitor

### ABSTRACT

In this work, spinel  $\text{NiCo}_2\text{O}_4$  is prepared by a facile sol–gel method with the effect of three different chelating agents including citric acid (CA), oxalic acid (OA) and ethylenediamine tetraacetic acid (EDTA) explored upon the fabrication methodology and resulting electrochemical and supercapacitor properties. The electrochemical measurements reveal that  $\text{NiCo}_2\text{O}_4$  prepared using OA exhibits ultrahigh specific capacitance of  $1254 \text{ F g}^{-1}$  at  $2 \text{ A g}^{-1}$  due to the resultant high specific surface area, while  $\text{NiCo}_2\text{O}_4$  prepared by EDTA exhibits the best rate capability and cycling stability owing to the subsequent large pore size. The obvious differences can be primarily ascribed to the use of the differing chelating agents which are shown, for the first time, to greatly affect the particle size, pore structure and specific surface area of the fabricated  $\text{NiCo}_2\text{O}_4$ . Such work is of fundamental importance and demonstrates that the tailoring of these different properties can be readily obtained through the use of differing chelating and is responsible for the observed differing electrochemical properties. Additionally, first-principles calculations were employed to investigate the electronic structure of  $\text{NiCo}_2\text{O}_4$ , which can help to further understand its excellent electrochemical behaviors. These results above provide a facile, cost-effective and high-performance strategy for supercapacitor electrode applications.

© 2014 Elsevier B.V. All rights reserved.

\* Corresponding author.

E-mail addresses: [xji@csu.edu.cn](mailto:xji@csu.edu.cn) (X. Ji), [c.banks@mmu.ac.uk](mailto:c.banks@mmu.ac.uk) (C.E. Banks).

## 1. Introduction

The development of efficient, clean, and sustainable energy technologies is being intensively pursued owing to the rapid growth of the global economy, the depletion of fossil fuels, and increasing environmental pollution [1]. Electrochemical energy storage technology comprising batteries, fuel cells, and supercapacitors is one of the most effective and practical technologies in many areas of application [2]. Supercapacitors (also named electrochemical capacitors or ultracapacitors) are receiving increasing consideration due to a combination of high power and reasonably high energy density, and they are ideally suited to the rapid storage and release of energy since they can provide high specific power, long cycle life, and fast charge/discharge processes [3,4]. Consequently, they are widely used in consumer electronics, memory back-up systems, hybrid electric vehicles, and industrial power management [5,6]. The energy stored in supercapacitors is either capacitive (electrochemical double layer capacitors) or pseudocapacitive (pseudocapacitors) in nature. The capacitive process is based on charge storage mechanisms at the surface of the electrode/electrolyte interface, while the pseudocapacitive process relies on redox reactions that occur in the electrode materials [7]. The most widely used active electrode materials are carbon [8,9], conducting polymers [10,11] and transition metal oxides [12–14]. Among them, transition metal oxides have attracted significant interest as active electrode materials for supercapacitors owing to the higher specific capacitance obtained from the Faradaic electrochemical reactions occurring on the surface of electrode materials.

Recently, various kinds of transition metal oxides have been explored as potential electrode materials for use in supercapacitors, primarily including RuO<sub>2</sub> [12,15], NiO [13,16], MnO<sub>2</sub> [14,17], Co<sub>3</sub>O<sub>4</sub> [18,19], etc. Among them, RuO<sub>2</sub> is the most prominent electrode material for supercapacitor applications because of its high specific capacitance, good electrical conductivity and reversible charge–discharge properties. Note that its highest specific capacitance ever reported was as high as 1580 F g<sup>−1</sup> [20]. Very recently, our group has also found that RuO<sub>2</sub> and its hybrid manifest outstanding supercapacitances under ultrafast charge and discharge with ultrahigh rate capability and remarkable cycling stability [21]. Despite many advantages, the high cost of RuO<sub>2</sub> is a limitation for extensive commercial acceptance, thus great efforts have been devoted to searching for inexpensive alternative materials with good capacitive characteristics similar to RuO<sub>2</sub>. Whereas, it is noteworthy that spinel NiCo<sub>2</sub>O<sub>4</sub> demonstrates an ultrahigh specific capacitance of 1400 F g<sup>−1</sup> under a mass loading of 0.4 mg cm<sup>−2</sup> from an epoxide-driven sol–gel process as reported by Hu et al. [22]. Spinel NiCo<sub>2</sub>O<sub>4</sub> not only has the advantages of low cost, environmental friendliness and abundant resources, but also possesses a much better electronic conductivity (at least two orders of magnitude higher) and higher electrochemical activity compared with NiO and Co<sub>3</sub>O<sub>4</sub> [23]. Therefore, spinel NiCo<sub>2</sub>O<sub>4</sub> is a potentially cost-effective replacement for RuO<sub>2</sub> as electrode materials for practical application in supercapacitors.

Currently, spinel NiCo<sub>2</sub>O<sub>4</sub> has been widely used in the fields of magnetic materials [23], electrocatalysts [24,25] and lithium ion batteries [22,26]. Whereas, it is only very recently that NiCo<sub>2</sub>O<sub>4</sub> has been used as a potential candidate for supercapacitive materials. So far, several kinds of methods including sol–gel [22,27], co-precipitation [28], hydrothermal [29] and electrodeposition [30] have been developed to synthesize NiCo<sub>2</sub>O<sub>4</sub>. Among them, sol–gel methods are considered to be one of the best choices for synthesizing high-performance electrode materials because of its many advantages such as homogeneity and purity in products, low-temperature synthesis, easy preparation of various morphologies,

low cost and convenient implement, and creation of very fine powders with high specific surface [31]. Note that the chelating agents play a vitally important role in the sol–gel process, the addition of chelating agent is to help give a uniform sol solution, and this particular merit is the molecule level mixing which facilitates the formation of homogeneous crystalline particles. Also, it is well-known that the particle size, pore structure and specific surface area of electrode materials can exert a great influence on the electrochemical properties, hence, it is significant for selecting the suitable chelating agents for the understanding of the effect of chelating agents on the electrochemical properties of electrode materials.

In this work, spinel NiCo<sub>2</sub>O<sub>4</sub> samples were prepared by a facile sol–gel method using three chelating agents, namely citric acid (CA), oxalic acid (OA) and ethylenediamine tetraacetic acid (EDTA). XRD, TGA, IR, HRTEM, SAED and BET were utilized to characterize the as-obtained samples. The effect of different chelating agents on the electrochemical properties of the NiCo<sub>2</sub>O<sub>4</sub> was, for the first time, investigated. As far as we are aware, no literature has been reported to investigate the effect of various chelating agents on the physicochemical and electrochemical properties of NiCo<sub>2</sub>O<sub>4</sub> prepared by sol–gel method. The electrochemical performances of the as-prepared NiCo<sub>2</sub>O<sub>4</sub> were measured by cyclic voltammetry (CV), galvanostatic current charge–discharge and electrochemical impedance spectroscopy (EIS), reveal that they exhibit excellent electrochemical properties. Additionally, first-principles calculations were used to investigate the electronic structure of NiCo<sub>2</sub>O<sub>4</sub> for further understanding its observed excellent electrochemical behaviors. This work demonstrates that through the tailoring/use of different chelating agents differing electrochemical properties/response of the fabricated NiCo<sub>2</sub>O<sub>4</sub> can be obtained. Such work is highly important fundamentally while providing a facile, cost-effective and high-performance strategy for supercapacitor electrode applications.

## 2. Experiment section

### 2.1. Materials and chemicals

All the chemicals used in the experiments were analytical grade and were used without further purification. Ni(Ac)<sub>2</sub>·4H<sub>2</sub>O (analytical grade) was purchased from Fengchuan Chemical Reagent Co., Ltd, Tianjin. Citric acid (analytical grade), ethylenediamine tetraacetic acid (analytical grade) and Co(Ac)<sub>2</sub>·4H<sub>2</sub>O (analytical grade) were bought from Xilong Chemical Co., Ltd. Oxalic acid (analytical grade) was obtained from the Hengxing Co., Ltd, Tianjin. All solutions were prepared with distilled water of resistivity not less than 18.2 MΩ cm (Synergy UV, Millipore).

### 2.2. Preparation of NiCo<sub>2</sub>O<sub>4</sub>

#### 2.2.1. CA-assisted sol–gel method

Ni(Ac)<sub>2</sub>·4H<sub>2</sub>O (0.05 M) and Co(Ac)<sub>2</sub>·4H<sub>2</sub>O (0.1 M) were first dissolved in distilled water (100 mL) and mixed well with each other. Citric acid solution (0.3 M, 100 mL) was then slowly added to the mixed solution at room temperature under constant magnetic stirring. The obtained mixture was stirred overnight and then the solution was evaporated at 80 °C until the gel was formed. The gel was subsequently dried and ground to obtain the precursor powder. Finally, the precursor powder was further annealed at 375 °C for 2 h in air.

#### 2.2.2. OA-assisted sol–gel method

Firstly, Ni(Ac)<sub>2</sub>·4H<sub>2</sub>O (0.05 M) and Co(Ac)<sub>2</sub>·4H<sub>2</sub>O (0.1 M) were dissolved in distilled water (100 mL) and mixed well with each

other. Then, an ethanol solution of oxalic acid (0.15 M, 100 mL) was slowly added to the mixed solution at room temperature under constant magnetic stirring. The obtained mixture was stirred overnight and then the solution was evaporated at 80 °C until the gel was formed. Subsequently, the gel was dried and ground to obtain the precursor powder. Lastly, the precursor powder was further annealed at 320 °C for 2 h in air.

### 2.2.3. EDTA-assisted sol–gel method

$\text{Ni}(\text{Ac})_2 \cdot 4\text{H}_2\text{O}$  (0.05 M) and  $\text{Co}(\text{Ac})_2 \cdot 4\text{H}_2\text{O}$  (0.1 M) were first dissolved in distilled water (100 mL) and mixed well with each other. Meanwhile, EDTA (0.15 M) was dissolved in distilled water (100 mL), and the ammonia was added dropwise to maintain the constant pH at 6.5. Then, the former mixed solution was slowly added to the EDTA ammonium solution at room temperature under constant magnetic stirring and the constant pH = 6.5 was maintained via dropwise addition of ammonia during this process. The obtained mixture was stirred overnight and then the solution was evaporated at 80 °C until the gel was formed. The gel was subsequently dried and ground to obtain the precursor powder. Finally, the precursor powder was further annealed at 400 °C for 2 h in air.

## 2.3. Materials characterization

The X-ray diffraction (XRD) patterns of the samples were obtained on a RigakuD/max 2550 VB<sup>+</sup> 18 kW X-ray diffractometer with Cu Ka radiation at a scanning rate of 0.1° 2θ s<sup>-1</sup>. Transmission electron microscopy (TEM, JEM-2100F), High resolution transmission electron microscopy (HRTEM, JEM-2100F) and the corresponding selected area electron diffraction (SAED) were used to characterize the morphology and structure of the samples. The chemical structure of the samples was examined by using the Fourier transform infrared spectrophotometer (FT-IR, AVTATAR, 370) in the frequency range from 400 cm<sup>-1</sup>–4000 cm<sup>-1</sup> with KBr as a reference. Thermogravimetric analysis (TGA) data were collected on a thermal analysis instrument (NETZSCH STA449F3) at a heating rate of 10 °C min<sup>-1</sup> from room temperature to 800 °C in air. The Brunauer–Emmett–Teller (BET, BELSORP-MINIII) specific surface area was obtained from the  $\text{N}_2$  adsorption/desorption isotherm recorded at 77 K and the pore size distribution was evaluated by using the Barrett–Joyner–Halenda (BJH) model.

## 2.4. Electrochemical characterization

The working electrodes were fabricated by first mixing  $\text{NiCo}_2\text{O}_4$ , acetylene black, and polyvinylidene difluoride (PVDF) with a weight ratio of 70:20:10 and the prepared mixture were then pressed onto a foam nickel under a pressure of 10 MPa for 30 s. The loading mass of the electroactive materials was around 1.0 mg cm<sup>-2</sup>. When used as a current collector, foam nickel was first immersed in 0.1 M HCl solution for 24 h, and then rinsed in an ultrasonic bath respectively with acetone and ethanol three times. Finally, it was dried in a vacuum oven at 70 °C for 10 h. A three electrode system consisted of the fabricated working electrode, platinum counter electrode and Hg/HgO reference electrode was employed in 2 M KOH aqueous solution. All measurements including cyclic voltammetry (CV), galvanostatic current charge–discharge and electrochemical impedance spectroscopy (EIS) were carried out on a Modulab (Solartron Analytical) electrochemical workstation.

## 2.5. First principle calculations

First-principles calculations were carried out with the spin-polarized Generalized Gradient Approximation (GGA) using the

Perdew–Burke–Ernzerh (PBE) of exchange-correlation parameterization to Density Functional Theory (DFT) using CASTEP program. A plane-wave basis with a kinetic energy cutoff was 300 eV. The electronic minimization parameters of total energy/atom convergence tolerance and eigen-energy convergence were respectively  $0.2 \times 10^{-5}$  and  $0.5385 \times 10^{-6}$  eV. The density mixing parameters of charge density mixing amplitude, cut-off energy for mixing and charge density mixing g-vector were 0.5000, 300.0 eV and 1.5001 Å<sup>-1</sup>, respectively.

## 3. Results and discussion

XRD technique is a very useful tool to determine the phase, crystallinity and purity of samples prepared under various conditions. Fig. 1a exhibits the XRD patterns of as-prepared  $\text{NiCo}_2\text{O}_4$  prepared by different chelating agents. All the peaks in the three patterns match the calculated pattern (Fig. 1b) very well, including the peak positions and intensities. No peaks from other crystallized phases have been detected, which is consistent with the TGA and FT-IR results, showing the formation of pure  $\text{NiCo}_2\text{O}_4$  product after low-temperature annealing treatment. The average crystal sizes of  $\text{NiCo}_2\text{O}_4$  prepared by CA, OA and EDTA assisted sol–gel method are respectively determined to be 16.6, 11.1 and 19.2 nm, which can be calculated by using the following Scherer's formula [32]:

$$D = (0.89 \times \lambda) / (\beta \times \cos \theta) \quad (1)$$

where  $D$  is the crystalline size,  $\lambda$  is the wavelength of X-rays emitted from the target,  $\theta$  is the Bragg diffraction angle of the diffraction peaks, and  $\beta$  is the full width at half maximum (FWHM) of the diffraction peak. The order of the average crystal sizes is (3) > (1) > (2), which can be interpreted from the XRD patterns in which the width of the diffraction peak is narrower and the shape of peak is sharper. The crystal sizes are further confirmed by TEM and HRTEM. These data indicate that the chelating agents have a great effect on obtaining excellent phase purity, crystal size and crystallinity of the  $\text{NiCo}_2\text{O}_4$ , thus influencing the electrochemical properties of the products. Fig. 1c and d manifests the crystallographic structure of cubic phase  $\text{NiCo}_2\text{O}_4$  (space group Fd3m), in which the Ni atoms occupy the octahedral sites and the Co atoms are distributed over both octahedral and tetrahedral sites [33].

In order to understand the weight loss with the temperature during the calcination process and determine the calcination temperature of the samples, the TGA of the  $\text{NiCo}_2\text{O}_4$  precursors prepared by CA, OA and EDTA was performed, as demonstrated in Fig. 2a–c. The TGA curve of  $\text{NiCo}_2\text{O}_4$  precursor prepared by CA is shown in Fig. 2a. The first significant weight loss occurs between 160 and 230 °C followed by the strong endothermic peak at about 174 and 207 °C, and this can be ascribed to the loss of crystal water from the metal citrate and the decomposition of metal citrate complex [34]. The second weight loss occurs between 330 and 370 °C with the strong endothermic peak at about 350 and 363 °C, which can be attributed to the complete decomposition of the metal precursor and the formation of  $\text{NiCo}_2\text{O}_4$ . Fig. 2b manifests the TGA curve of  $\text{NiCo}_2\text{O}_4$  precursor prepared by OA. The first obvious weight loss occurs in the temperature range of 170–210 °C followed by an endothermic peak at 200 °C, which is ascribed to the loss of crystal water. In the second temperature range of 280–314 °C, the sharp weight loss with a strong endothermic peak at about 302 °C indicates the decomposition of the metal oxalate and the formation of  $\text{NiCo}_2\text{O}_4$ . As displayed in Fig. 3c, the TGA curve of  $\text{NiCo}_2\text{O}_4$  precursor prepared by EDTA is presented. The curve also shows two steps of weight loss. The first weight loss (before 200 °C) can be attributed to the removal of absorbed and crystal water, and the second distinct weight loss in the temperature range of

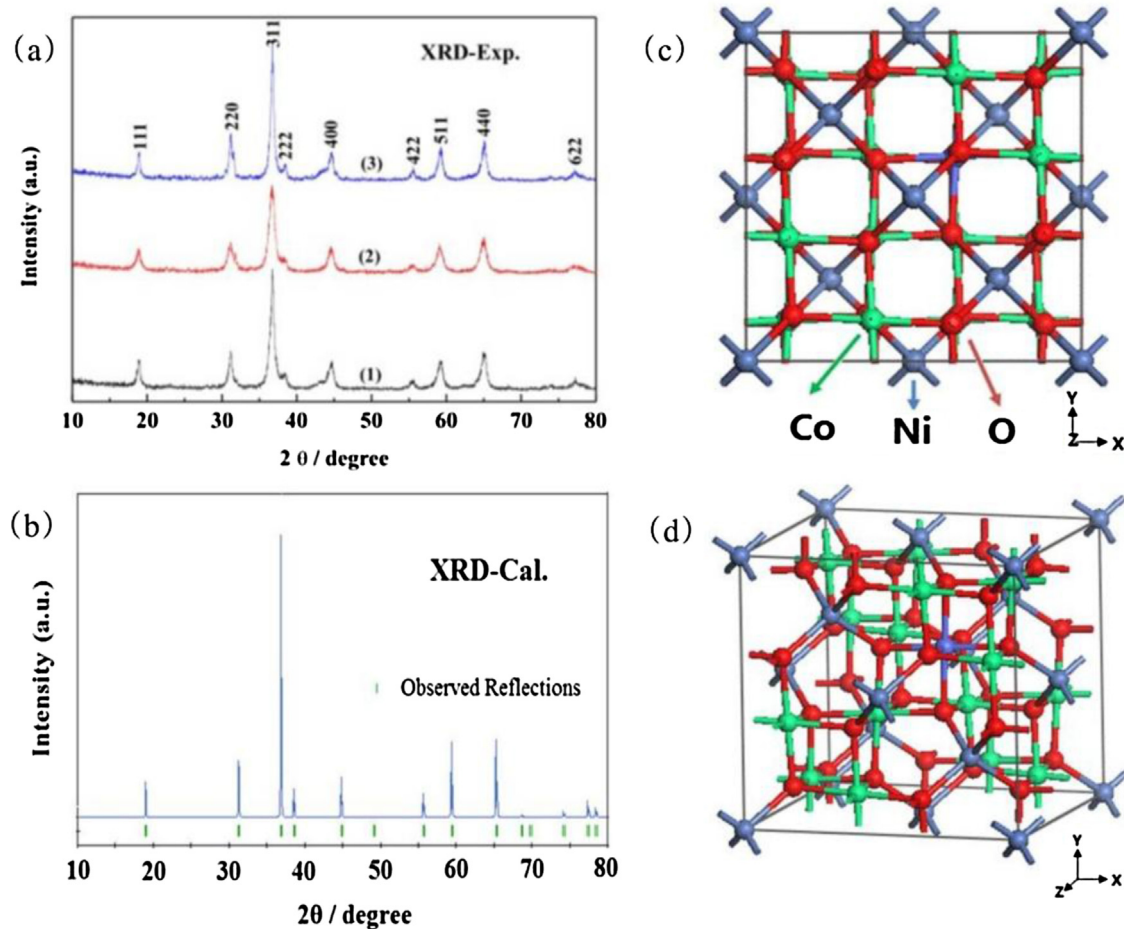


**Fig. 1.** (a) Experimental XRD patterns of NiCo<sub>2</sub>O<sub>4</sub> prepared by different chelating agents: (1) CA; (2) OA; (3) EDTA. (b) XRD patterns generated from first-principles calculations of NiCo<sub>2</sub>O<sub>4</sub>. (c, d) Crystal structure of spinel NiCo<sub>2</sub>O<sub>4</sub>.

265–395 °C can be ascribed to the decomposition of the metal precursor and the burnout of organics. When the temperature is close to 400 °C, the speed of weight loss is very slow and the weight remains constant regardless of further temperature increment, suggesting the formation of NiCo<sub>2</sub>O<sub>4</sub> crystal. From the TGA analysis, we can determine the calcination temperature of the samples required for the formation of spinel NiCo<sub>2</sub>O<sub>4</sub> is respectively 375, 320 and 400 °C for CA, OA and EDTA, and the difference of calcination temperature is due to the use of the various chelating agents, which is elucidated in later analysis.

FT-IR spectra were used to investigate the structural molecular changes and confirm the formation of NiCo<sub>2</sub>O<sub>4</sub> after annealing. The FT-IR spectra of NiCo<sub>2</sub>O<sub>4</sub> precursor and NiCo<sub>2</sub>O<sub>4</sub> prepared by CA are shown in Fig. 2d. The peaks at around 3426 and 1625 cm<sup>-1</sup> are respectively corresponding to –OH stretching and bending modes of absorbed water molecules, and the peak at 1726 cm<sup>-1</sup> is attributed to C=O stretching vibration of the carboxyl group. Furthermore, the peaks at around 1401, 1220 and 1077 cm<sup>-1</sup> are respectively corresponding to –OH bending vibration in COOH, C–O–C and C–O stretching vibration due to the presence of citric acid molecules. It is evident from the IR analysis of the precursor that the peaks assigned to citric acid molecules disappear after annealing. The spectrum exhibits the characteristic absorption peaks of metal–oxygen vibrations at 656 and 563 cm<sup>-1</sup> [23,35]. The broad peak at 3426 cm<sup>-1</sup> and the weak peak at 1625 cm<sup>-1</sup> are due to adsorbed water. As demonstrated in Fig. 2e and f, it is not surprising to see that a large

number of characteristic FT-IR absorption peaks which are evident in NiCo<sub>2</sub>O<sub>4</sub> precursors prepared by OA and EDTA are absent in the annealed samples. The NiCo<sub>2</sub>O<sub>4</sub> prepared by OA and EDTA demonstrate almost the same FT-IR spectra as that of NiCo<sub>2</sub>O<sub>4</sub> prepared by CA, which is the same as that reported by N. S. Chaubal [36].

To investigate the morphology, nanoparticle size and crystalline characteristics of NiCo<sub>2</sub>O<sub>4</sub>, TEM, HRTEM and the corresponding SAED studies (Fig. 3) were performed. Fig. 3a and b shows the TEM and HRTEM images of NiCo<sub>2</sub>O<sub>4</sub> prepared by CA, and the NiCo<sub>2</sub>O<sub>4</sub> is composed of lots of uniform nanoparticles with a size distribution of 10–20 nm, which is consistent with the result obtained from the XRD analysis. The inset in Fig. 3a is the corresponding SAED pattern, which reveals the polycrystalline nature of the NiCo<sub>2</sub>O<sub>4</sub> nanoparticles. Fig. 3c exhibits a HRTEM image of the NiCo<sub>2</sub>O<sub>4</sub> nanoparticles, and the observed interplanar spacing is measured to be 0.29 nm, which matches well with the (220) lattice plane of NiCo<sub>2</sub>O<sub>4</sub>. Fig. 3d–f shows the TEM, HRTEM images and the corresponding SAED pattern of NiCo<sub>2</sub>O<sub>4</sub> prepared by OA. Fig. 3d and e exhibit that NiCo<sub>2</sub>O<sub>4</sub> consists of many tiny uniform nanoparticles with a size range of 8–12 nm, which is the same as the result obtained from the XRD analysis. The tiny nanoparticles of NiCo<sub>2</sub>O<sub>4</sub> indicate the high specific surface area, which is beneficial for the enhancement of the pseudocapacitance of active materials [37]. Additionally, the SAED pattern is shown in Fig. 3d, which suggests the polycrystalline nature of NiCo<sub>2</sub>O<sub>4</sub> nanoparticles. The interplanar spacing is 0.29 nm, which is in an excellent agreement with

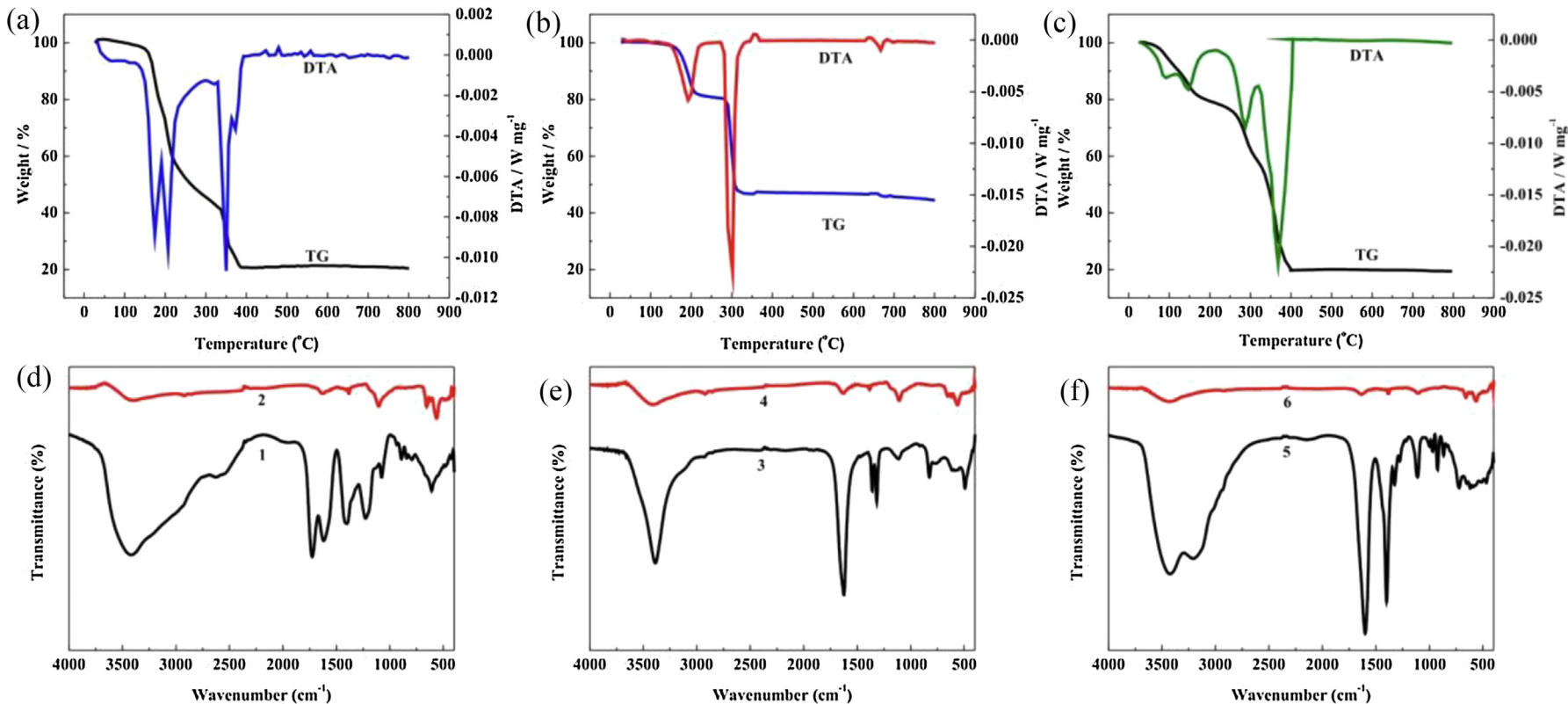


**Fig. 2.** TGA curves of the  $\text{NiCo}_2\text{O}_4$  precursors prepared by different chelating agents: (a) Citric acid; (b) Oxalic acid; (c) EDTA. FT-IR spectra of  $\text{NiCo}_2\text{O}_4$  precursors prepared by different chelating agents: (d) CA 2; (e) OA 4; (f) EDTA 6 and  $\text{NiCo}_2\text{O}_4$  prepared by different chelating agents: (d) CA 2; (e) OA 4; (f) EDTA 6.

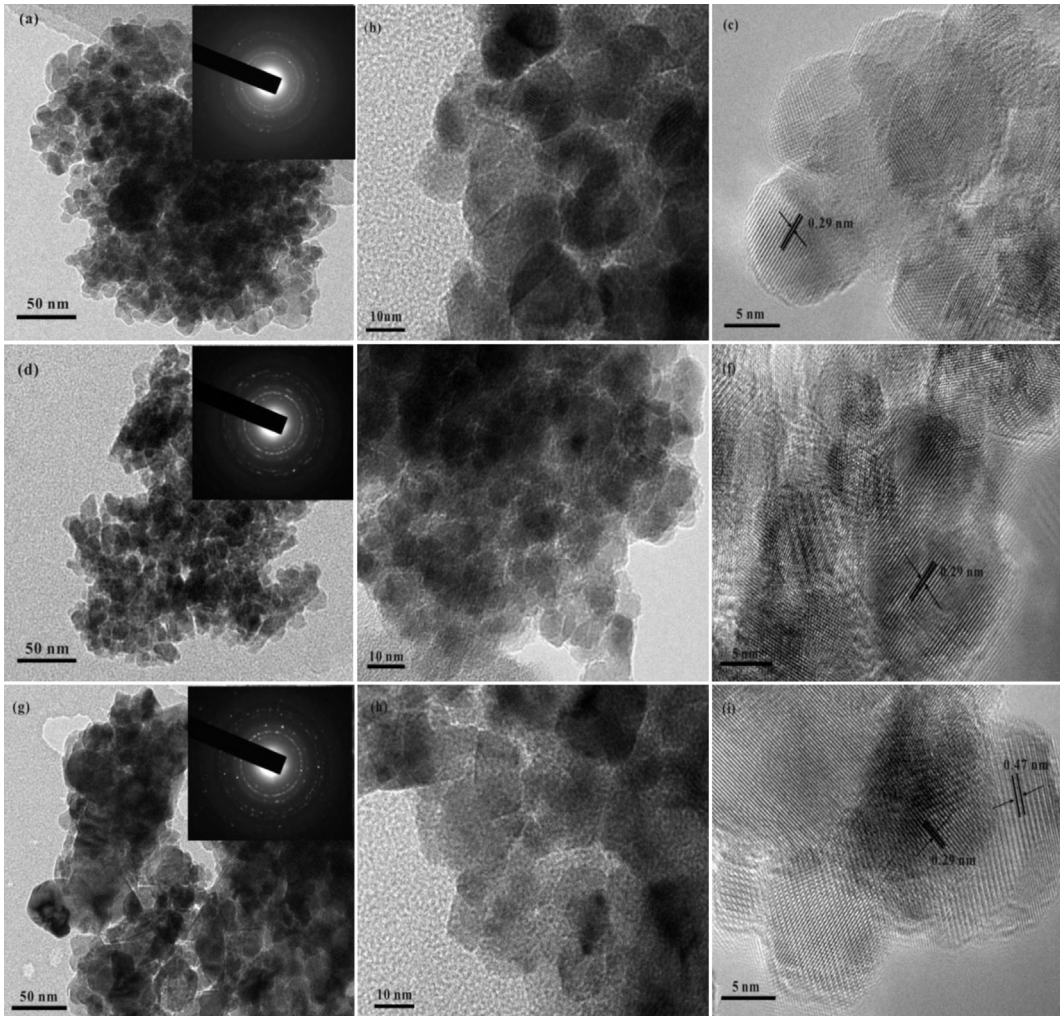


**Fig. 3.** TEM images of  $\text{NiCo}_2\text{O}_4$  prepared by different chelating agents: (a) CA; (d) OA; (g) EDTA; inset: corresponding SAED patterns. HRTEM images of  $\text{NiCo}_2\text{O}_4$  prepared by different chelating agents: (b and c) CA; (e and f) OA; (h and i) EDTA.

the (220) lattice plane of  $\text{NiCo}_2\text{O}_4$ . Fig. 3g–i displays the TEM, HRTEM images and the corresponding SAED pattern of the  $\text{NiCo}_2\text{O}_4$  prepared by EDTA. Fig. 3g and h manifest that  $\text{NiCo}_2\text{O}_4$  consists of many nanoparticles with a size range of 15–25 nm, and the observed result is the same as the XRD analysis. The inset in Fig. 3g is the SAED pattern, indicating the polycrystalline nature of  $\text{NiCo}_2\text{O}_4$  nanoparticles. The observed interplanar spacings from the HRTEM image (Fig. 3i) are measured to be 0.29 and 0.47 nm, which match well with the (220) and (111) lattice planes of  $\text{NiCo}_2\text{O}_4$ . From the comparison of TEM images for three samples, we can clearly observe the difference, especially for the particle sizes, resulting in the differing of pore structure and specific surface area, which is further confirmed by the following BET measurement. The difference of TEM images can be mainly due to the use of the various chelating agents.

The BET specific surface areas of the  $\text{NiCo}_2\text{O}_4$  prepared by sol–gel method with different chelating agents are determined by  $\text{N}_2$  adsorption–desorption isotherms at 77 K, and the corresponding pore size distributions are calculated by Barrett–Joyner–Halenda (BJH) method, as displayed in Fig. 4. Important structural parameters are derived from the isotherms and tabulated in Table 1. All the samples exhibit a hysteresis loop and the BET specific surface areas of the  $\text{NiCo}_2\text{O}_4$  prepared by CA, OA and EDTA are calculated to be 37.41, 61.149 and  $20.048 \text{ m}^2 \text{ g}^{-1}$ , respectively. The pore size

distributions of the samples are shown in inset of Fig. 4. Fig. 4a gives the main mesoporous structure of the  $\text{NiCo}_2\text{O}_4$  (CA) with a narrow and ordered pore-size distribution at  $\sim 5.29 \text{ nm}$ , and the pore volume is calculated as  $0.1142 \text{ cm}^3 \text{ g}^{-1}$ . As shown in Fig. 4b, the  $\text{NiCo}_2\text{O}_4$  (OA) manifests a sharp peak at  $\sim 1.88 \text{ nm}$  and wide peaks at 10.6 and  $19.0 \text{ nm}$ , which indicates that the pores of the  $\text{NiCo}_2\text{O}_4$  consist of a large number of micropores and mesopores, and the pore volume is up to  $0.2387 \text{ cm}^3 \text{ g}^{-1}$ . Such a pore structure is particularly favorable for supercapacitors because this type of structure with a high surface area and a large pore volume can facilitate the electrolyte ion diffusion and charge transfer, and thus provide more electroactive sites for energy storage. The  $\text{NiCo}_2\text{O}_4$  (EDTA) exhibits the main mesoporous structure with a narrow pore-size distribution at 2.4 and  $6.0 \text{ nm}$  and a wide pore-size distribution at 16.3 and  $25.8 \text{ nm}$  (Fig. 4c), and the pore volume is  $0.1389 \text{ cm}^3 \text{ g}^{-1}$ . This feature is of huge benefits for the transport and diffusion of electrolyte ions during the charge–discharge process in supercapacitors. Note that all  $\text{N}_2$  isotherms exhibit an obvious volume increase at relative pressure range of 0.85–1.0, and a certain number of macropores can be observed from the BJH pore size distribution curves. Moreover, we can see that the quantity of macropores for  $\text{NiCo}_2\text{O}_4$  (EDTA) is greater than  $\text{NiCo}_2\text{O}_4$  (CA) and  $\text{NiCo}_2\text{O}_4$  (OA). Due to the differences of BET specific surface area, pore volume and pore size distribution, it is reasonable to speculate

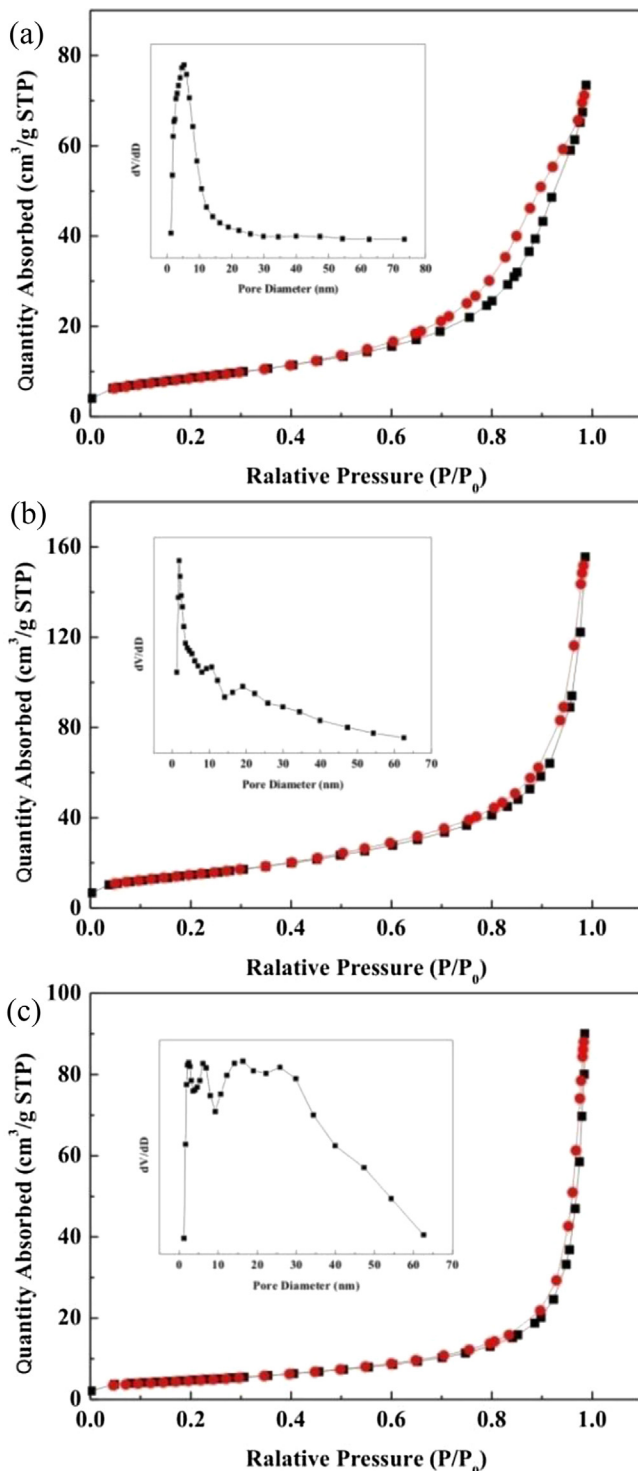


**Fig. 4.** Nitrogen adsorption and desorption isotherms of the NiCo<sub>2</sub>O<sub>4</sub> prepared by different chelating agents: (a) CA; (b) OA; (c) EDTA. The insets show the corresponding BJH pore size distributions.

that the NiCo<sub>2</sub>O<sub>4</sub> prepared by sol–gel method with different chelating agents will display different electrochemical performances.

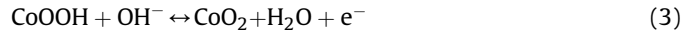
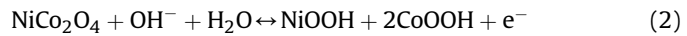
To evaluate the properties of the NiCo<sub>2</sub>O<sub>4</sub> electrodes prepared by sol–gel method with different chelating agents as supercapacitor electrodes, the detailed measurements and the comparison of the electrochemical performances are presented in Figs. 5

**Table 1**  
Structural parameters of spinel NiCo<sub>2</sub>O<sub>4</sub> prepared by different chelating agents.

Samples	BET specific surface area (m <sup>2</sup> g <sup>-1</sup> )	BH pore volume (cm <sup>3</sup> g <sup>-1</sup> )	BH pore size (nm)
NiCo <sub>2</sub> O <sub>4</sub> (CA)	37.41	0.1142	5.29
NiCo <sub>2</sub> O <sub>4</sub> (OA)	61.149	0.2387	1.88
NiCo <sub>2</sub> O <sub>4</sub> (EDTA)	20.048	0.1389	16.3

and 6, which exhibit the cyclic voltammetry (CV), galvanostatic current charge–discharge, cycling stability and electrochemical impedance spectroscopy (EIS).

Fig. 5a–c display CV measurements for the NiCo<sub>2</sub>O<sub>4</sub> electrodes prepared by CA, OA and EDTA, respectively. The CV was measured in 2 M KOH solution at potential intervals from 0 to 0.55 V at scanning rates of 5–100 mV s<sup>-1</sup>. The shapes of the CV curves clearly exhibit the pseudocapacitive behavior caused by electrochemical reactions. The redox peaks of the NiCo<sub>2</sub>O<sub>4</sub> electrodes originate mainly from the Faradaic reactions occurred in the electrode materials and the redox reactions in the alkaline electrolyte have two steps, which respectively correspond to the reversible reactions of Ni<sup>2+</sup>/Ni<sup>3+</sup> and Co<sup>3+</sup>/Co<sup>4+</sup> transitions associated with anions OH<sup>-</sup>. The redox reactions in the alkaline electrolyte are based on the following equations:



The oxidation peak potential of Ni<sup>2+</sup>/Ni<sup>3+</sup> and Co<sup>3+</sup>/Co<sup>4+</sup> transition at a scan rate of 10 mV s<sup>-1</sup> is respectively 0.51 V (1 M KOH, Hg/HgO) [38] and 0.515 V (1 M KOH, Hg/HgO) [39] as reported in the literature, which can explain why only a pair of redox peaks from the CV curves is actually observed. This is because the redox potential of Ni<sup>2+</sup>/Ni<sup>3+</sup> and Co<sup>3+</sup>/Co<sup>4+</sup> transitions is so close that it is difficult to tell them apart. As can be seen from the CV curves, the oxidation peak potential is 0.49 V (2 M KOH, Hg/HgO), which is close to the value of the literature. In addition, we can clearly observe that the position of the anodic and cathodic peaks shifts slightly with the 20-fold increase of the scan rate from 5 to 100 mV s<sup>-1</sup> as displayed in Fig. 5a–c, indicating a relatively low resistance of the electrode and good electrochemical reversibility [40]. Fig. 5d shows the comparison of the CV curves of the NiCo<sub>2</sub>O<sub>4</sub> electrodes prepared by CA, OA and EDTA at a scan rate of 50 mV s<sup>-1</sup>, from which we can learn that the order of the area under the CV curve of the NiCo<sub>2</sub>O<sub>4</sub> electrodes prepared by different chelating agents is OA > CA > EDTA. It is well-known that the specific capacitance is proportional to the area of the CV curve [41]. Therefore, the order of the specific capacitance of the NiCo<sub>2</sub>O<sub>4</sub> electrodes prepared by different chelating agents is OA > CA > EDTA, which can be further verified by the following charge–discharge measurements.

Fig. 5e–g respectively manifest the galvanostatic discharge curves of the NiCo<sub>2</sub>O<sub>4</sub> electrodes prepared by CA, OA and EDTA at various current densities with a potential range of 0–0.5 V. The nonlinear discharge curves and the voltage plateaus match well with the peaks observed from the CV curves, which further verifies the pseudocapacitance behavior of the NiCo<sub>2</sub>O<sub>4</sub> electrodes. The specific capacitance of the NiCo<sub>2</sub>O<sub>4</sub> electrodes can be calculated by using the following formula [42]:

$$C_m = (I \times \Delta t) / (\Delta V \times m) \quad (4)$$

where  $C_m$  (F g<sup>-1</sup>) is the specific capacitance of a single electrode,  $I$  (A) is the discharging current,  $\Delta t$  (s) is the discharging time,  $\Delta V$  (V)

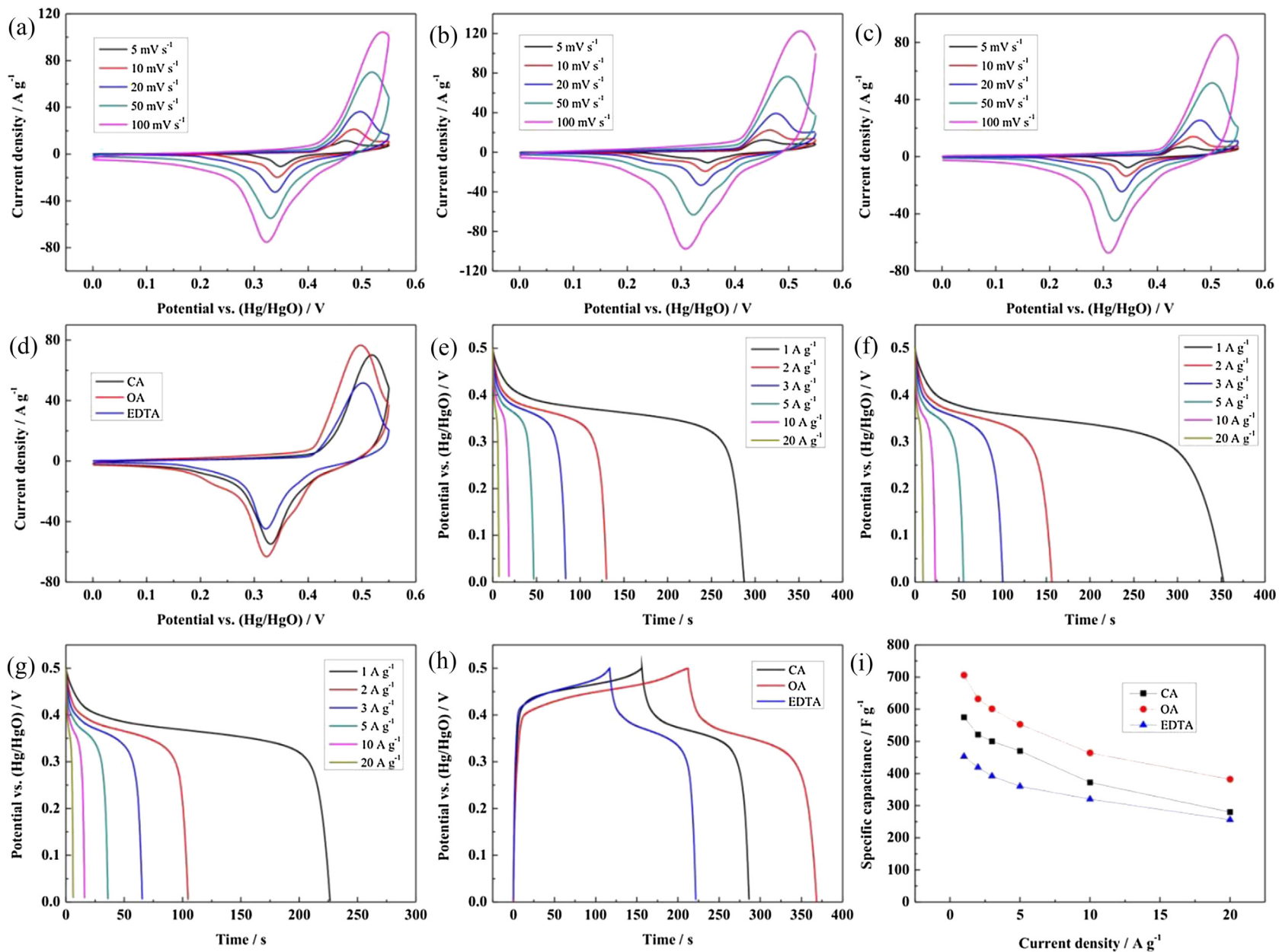


**Fig. 5.** (a–c) CV curves of the  $\text{NiCo}_2\text{O}_4$  electrodes prepared by CA, OA and EDTA at various scan rates. (d) Comparison of CV curves of the  $\text{NiCo}_2\text{O}_4$  electrodes prepared by CA, OA and EDTA at a scan rate of 50  $\text{mV s}^{-1}$ . (e–g) Galvanostatic discharge curves of the  $\text{NiCo}_2\text{O}_4$  electrodes prepared by CA, OA and EDTA at various current densities. (h) Comparison of galvanostatic charge and discharge curves of the  $\text{NiCo}_2\text{O}_4$  electrodes prepared by CA, OA and EDTA at a current density of 2  $\text{A g}^{-1}$ . (i) Comparison of the specific capacitance change of the  $\text{NiCo}_2\text{O}_4$  electrodes prepared by CA, OA and EDTA as a function of current density.

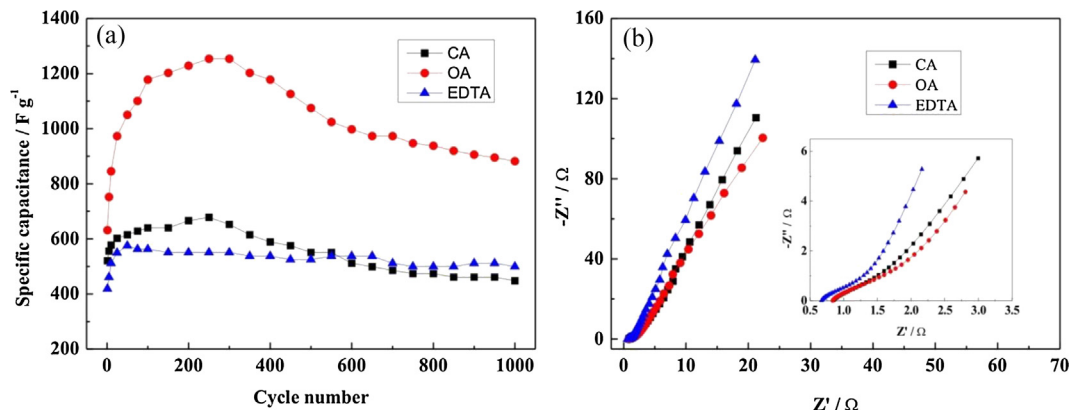


**Fig. 6.** (a) Comparison of the cycling stability of the  $\text{NiCo}_2\text{O}_4$  electrodes prepared by CA, OA and EDTA at a current density of  $2 \text{ A g}^{-1}$ . (b) Comparison of Nyquist impedance plots of the  $\text{NiCo}_2\text{O}_4$  electrodes prepared by CA, OA and EDTA, and the inset shows a magnification of the high-frequency region of the impedance spectra.

is the potential drop during discharge, and  $m$  (g) is the mass of active materials. The specific capacitances of the  $\text{NiCo}_2\text{O}_4$  electrodes prepared by CA, OA and EDTA are summarized in Table 2. The specific capacitance of the  $\text{NiCo}_2\text{O}_4$  prepared by CA is calculated to be  $575, 521, 500, 470, 372$ , and  $280 \text{ F g}^{-1}$  at current densities of  $1, 2, 3, 5, 10$ , and  $20 \text{ A g}^{-1}$ , and the capacity retention rate (compared with  $1 \text{ A g}^{-1}$ ) is  $64.7\%$  and  $48.7\%$  at current densities of  $10$  and  $20 \text{ A g}^{-1}$ , respectively. Compared to the  $\text{NiCo}_2\text{O}_4$  electrode prepared by CA shown in Fig. 5h and i, the  $\text{NiCo}_2\text{O}_4$  electrode prepared by OA manifests higher capacitance and better rate capability, which is in agreement with the result of the CV curves. The specific capacitance is calculated to be  $706, 632, 601, 553, 464$ , and  $382 \text{ F g}^{-1}$  at current densities of  $1, 2, 3, 5, 10$ , and  $20 \text{ A g}^{-1}$ , and the capacity retention rate (compared with  $1 \text{ A g}^{-1}$ ) is respectively up to  $65.7\%$  and  $54.1\%$  at current densities of  $10$  and  $20 \text{ A g}^{-1}$  (Table 3). This is due to the higher BET specific surface area and larger pore volume, which increase electrolyte/electrode contact areas and hence provide more active sites for fast faradaic redox reactions, as is mentioned above. As for the  $\text{NiCo}_2\text{O}_4$  electrode prepared by EDTA, the specific capacitance is calculated to be  $453, 419, 392, 360, 320$ , and  $256 \text{ F g}^{-1}$  at current densities of  $1, 2, 3, 5, 10$ , and  $20 \text{ A g}^{-1}$ , respectively. Although the specific capacitance of the  $\text{NiCo}_2\text{O}_4$  electrode prepared by EDTA is relatively lower than that of  $\text{NiCo}_2\text{O}_4$  electrodes prepared by CA and OA, the capacity retention rate (compared with  $1 \text{ A g}^{-1}$ ) is the highest among them, and it is respectively up to  $70.6\%$  and  $56.5\%$  at current densities of  $10$  and  $20 \text{ A g}^{-1}$  (Table 3). This is probably ascribed to this unique mesoporous structure with a relatively larger pore size, which can serve as the ion-buffering reservoirs for  $\text{OH}^-$  ions to minimize the diffusion distance to the interior surfaces and accelerate the kinetic process of  $\text{OH}^-$  ions diffusion in the electrode, thus enhancing the electrochemical kinetics [43].

To evaluate the cycling stability of the  $\text{NiCo}_2\text{O}_4$  electrodes prepared by CA, OA and EDTA, the tests were conducted at a constant

current density of  $2 \text{ A g}^{-1}$  in the potential range of  $0$ – $0.5 \text{ V}$  in  $2 \text{ M KOH}$  solution for 1000 cycles. As shown in Fig. 6a, the specific capacitance of all the three samples increases at first, instead of decreasing as in most cycling stability tests in the literature, and then decreases with cycling numbers. This is ascribed to the cycling-induced improvement in the surface wetting of the electrode, leading to more electroactive surface areas. Similar phenomena have also been reported by other groups [22,28]. Also we note that it is different from the results reported by Hu et al. [44,45] where they conclude that the  $\text{NiCo}_2\text{O}_4$  particle size has a great effect on the cycling activation time, and the larger size of  $\text{NiCo}_2\text{O}_4$  crystals are, the longer electrochemical activation time is needed. In our case, the specific capacitance of the  $\text{NiCo}_2\text{O}_4$  electrode prepared by CA reaches a maximum value of  $678 \text{ F g}^{-1}$  at a cycle number of 250 and still maintains at a high value of  $448 \text{ F g}^{-1}$  after 1000 cycles (retaining  $86\%$  of its initial capacitance and  $66.1\%$  of its activated maximum capacitance). Whereas, it is noted that the specific capacitance of the  $\text{NiCo}_2\text{O}_4$  electrode prepared by OA reaches an ultrahigh value of  $1254 \text{ F g}^{-1}$  at a cycle number of 300 and still maintains even at a high value of  $882 \text{ F g}^{-1}$  after 1000 cycles (retaining  $139.6\%$  of its initial capacitance and  $70.4\%$  of its activated maximum capacitance). As for the  $\text{NiCo}_2\text{O}_4$  electrode prepared by EDTA, the specific capacitance reaches a maximum value of  $576 \text{ F g}^{-1}$  at a cycle number of 50 and still maintains even at a high value of  $500 \text{ F g}^{-1}$  after 1000 cycles (retaining  $119.3\%$  of its initial capacitance and  $86.8\%$  of its activated maximum capacitance). From the comparison of the cycling stability of the  $\text{NiCo}_2\text{O}_4$  electrodes prepared by CA, OA and EDTA, it is not hard to observe that the  $\text{NiCo}_2\text{O}_4$  electrode prepared by OA needs more cycling numbers to reach the maximum specific capacitance, and this is because the smaller pore size of the  $\text{NiCo}_2\text{O}_4$  electrode prepared by OA needs longer time to reach the complete activation. Additionally, we can clearly see that the  $\text{NiCo}_2\text{O}_4$  electrodes prepared by EDTA and OA have better cycling stability in comparison with the  $\text{NiCo}_2\text{O}_4$

**Table 2**  
The initial specific capacitance and activated maximum specific capacitance of the  $\text{NiCo}_2\text{O}_4$  electrodes prepared by CA, OA and EDTA at current densities of  $1$ – $20 \text{ A g}^{-1}$  and  $2 \text{ A g}^{-1}$ , respectively.

Samples	Initial specific capacitance ( $\text{F g}^{-1}$ )						Activated maximum specific capacitance ( $\text{F g}^{-1}$ ) $2 \text{ A g}^{-1}$
	$1 \text{ A g}^{-1}$	$2 \text{ A g}^{-1}$	$3 \text{ A g}^{-1}$	$5 \text{ A g}^{-1}$	$10 \text{ A g}^{-1}$	$20 \text{ A g}^{-1}$	
$\text{NiCo}_2\text{O}_4$ (CA)	575	521	500	470	372	280	678
$\text{NiCo}_2\text{O}_4$ (OA)	706	632	601	553	464	382	1254
$\text{NiCo}_2\text{O}_4$ (EDTA)	453	419	392	360	320	256	576

**Table 3**

The rate capacity retention of the  $\text{NiCo}_2\text{O}_4$  electrodes prepared by CA, OA and EDTA at current densities of  $10 \text{ A g}^{-1}$  and  $20 \text{ A g}^{-1}$  (compared with  $1 \text{ A g}^{-1}$ ), and the cycling capacity retention of the  $\text{NiCo}_2\text{O}_4$  electrodes prepared by CA, OA and EDTA at a current density of  $2 \text{ A g}^{-1}$  for 1000 cycles (compared with the initial specific capacitance and activated maximum specific capacitance).

Samples	Rate capacity retention (%)		Cycling capacity retention (%)	
	$10 \text{ A g}^{-1}$	$20 \text{ A g}^{-1}$	Initial specific capacitance	Activated maximum specific capacitance
$\text{NiCo}_2\text{O}_4$ (CA)	64.7	48.7	86.0	66.1
$\text{NiCo}_2\text{O}_4$ (OA)	65.7	54.1	139.6	70.4
$\text{NiCo}_2\text{O}_4$ (EDTA)	70.6	56.5	119.4	86.8

electrode prepared by CA. The superior cycling stability can probably be attributed to the differences in the pore structures. The mesoporous structure with the larger pore size and pore volume is reckoned to alleviate the volume changes during  $\text{OH}^{-1}$  ions insertion/extraction processes while cycling. Therefore, the selection of chelating agents is a particularly key factor in determining the performance of the electrode materials.

EIS was performed by using  $2 \text{ M KOH}$  as an electrolyte to further evaluate the electrochemical performance, and the EIS data were analyzed by using Nyquist plots. Nyquist plots of the  $\text{NiCo}_2\text{O}_4$  electrodes prepared by CA, OA and EDTA in the frequency range (100 kHz–0.1 Hz) are displayed in Fig. 6b. In the high frequency region, the real axis intercept represents the internal resistance, including the sum of the contact resistance of the interface between active material and current collector, the intrinsic resistance of the active material and the ionic resistance of the electrolyte, and the semicircle corresponds to the charge transfer resistance [46]. In Nyquist plots, all the three types of  $\text{NiCo}_2\text{O}_4$  electrodes manifest a small real axis intercept and negligible semicircle. This indicates the low interfacial resistance between current collector and active material, active material resistance and electrolyte resistance, as well as low charge transfer resistance. This is mainly due to the high electrical conductivity of  $\text{NiCo}_2\text{O}_4$ , which is in agreement with the CV analysis. Also, this is further confirmed by the result obtained from the first-principles calculations. Obviously, we can observe from Fig. 7b that the  $\text{NiCo}_2\text{O}_4$  electrode prepared by EDTA shows lower internal resistance and charge transfer resistance than the  $\text{NiCo}_2\text{O}_4$  electrodes prepared by CA and OA, which can explain why the  $\text{NiCo}_2\text{O}_4$  prepared by EDTA remains better rate capability than the  $\text{NiCo}_2\text{O}_4$  prepared by CA and OA due to the fact that the resistance is an important factor in determining the rate performance for supercapacitor electrode materials [47]. In the low frequency region, the straight line represents the diffusive resistance of the electrolyte ions in host materials. The Nyquist plot is a vertical line for an ideal electrode material. The more vertical the line is, the better the capacitive behavior is [48]. Compared with the  $\text{NiCo}_2\text{O}_4$  electrodes prepared by CA and OA, the  $\text{NiCo}_2\text{O}_4$  electrode prepared by EDTA manifests a more vertical line leaning to imaginary axis more than  $45^\circ$  at a low frequency region, suggesting the more facile electrolyte ions diffusion to the active material and more ideal capacitor behavior due to its unique mesoporous structure, which further verifies that the  $\text{NiCo}_2\text{O}_4$  electrode prepared by EDTA can remain superior rate capability and cycling stability compared to the  $\text{NiCo}_2\text{O}_4$  electrodes prepared by CA and OA.

The high electrical conductivity of the  $\text{NiCo}_2\text{O}_4$  as mentioned above was confirmed by using the first-principles calculations based on the density functional theory to investigate its electronic structures. According to the reported literature [49],  $\text{NiCo}_2\text{O}_4$  has a much higher electrical conductivity than  $\text{Co}_3\text{O}_4$ , and Ni doping improves the electrical conductivity from  $0.31 \times 10^{-4} \text{ S cm}^{-1}$  for  $\text{Co}_3\text{O}_4$  to  $0.12 \text{ S cm}^{-1}$  for  $\text{NiCo}_2\text{O}_4$ . In order to compare the electrical

conductivity of  $\text{Co}_3\text{O}_4$  and  $\text{NiCo}_2\text{O}_4$ , the band structures and density of states of  $\text{Co}_3\text{O}_4$  and  $\text{NiCo}_2\text{O}_4$  were investigated, as illustrated in Fig. 7. From Fig. 7a and b, it is clearly seen that the band structures of  $\text{Co}_3\text{O}_4$  and  $\text{NiCo}_2\text{O}_4$  show the obvious differences after substitution of  $\text{Co}^{2+}$  with  $\text{Ni}^{2+}$  in  $\text{Co}_3\text{O}_4$ . The calculated band gaps of  $\text{Co}_3\text{O}_4$  and  $\text{NiCo}_2\text{O}_4$  from Fig. 7c are 1.1026 and 0.2462 eV, respectively. It is well-known that the lower band gap means the higher electrical conductivity [50]. Thus,  $\text{NiCo}_2\text{O}_4$  exhibits higher electrical conductivity than  $\text{Co}_3\text{O}_4$  via substitution of  $\text{Co}^{2+}$  with  $\text{Ni}^{2+}$  in  $\text{Co}_3\text{O}_4$ . In addition, the apparent differences of density of states near Fermi surface for  $\text{Co}_3\text{O}_4$  and  $\text{NiCo}_2\text{O}_4$  can be clearly observed in Fig. 7d. The value of density of states near Fermi surface for  $\text{NiCo}_2\text{O}_4$  ( $17.0 \text{ electrons eV}^{-1}$ ) is far higher than  $\text{Co}_3\text{O}_4$  ( $0.28 \text{ electrons eV}^{-1}$ ). According to quantum theory, only electrons near the Fermi level can contribute to current in the external electric field, and hence the electrical conductivity of material is proportional to the electrons occupied in the Fermi level [51]. Therefore, the electrical conductivity of Ni-substituted  $\text{Co}_3\text{O}_4$  ( $\text{NiCo}_2\text{O}_4$ ) is greatly improved. Such a huge increase of the electrical conductivity of  $\text{NiCo}_2\text{O}_4$  can reasonably explain its low resistance, and thus greatly enhance its supercapacitive performances, which can be further verified from the comparison of electrochemical performances of  $\text{Co}_3\text{O}_4$  and  $\text{NiCo}_2\text{O}_4$  reported in the literature [37,52].

From the above discussion we can conclude that chelating agents play an important role in the preparation of spinel  $\text{NiCo}_2\text{O}_4$  nanoparticles. To further understand the effect of chelating agents on the electrochemical properties, a synthesis scheme is proposed in Fig. 8. In this process of sol–gel synthesis, it can be divided into two steps. The first step is that these chelating agents (citric acid, oxalic acid or EDTA) bind with cations ( $\text{Ni}^{2+}$  and  $\text{Co}^{2+}$ ) to form very stable chelating complexes due to the chelation between complex cations and a hydroxycarboxylic acid [53]. Adding these chelating agents to a molecularly mixed solution of nickel and cobalt ions will result in an immediate and strong bonding of the cations with the coordinating centers in the chelating agents to form micelles in which the cations are trapped in an organic environment, which hamper selective precipitation of the cations during the solvent evaporation. After prolonged heating, the viscous polymeric mass gets partially carbonized, providing a substrate in which the cations find themselves embedded. The second step is that the chelating complexes decompose in heating and air condition and form the spinel  $\text{NiCo}_2\text{O}_4$ . During this step, the chelating agents as a fuel help to progress the synthesis at relatively low temperatures [54,55]. In order to remove the chelating agents and create a porous structure, thermal decomposition was further conducted. During the calcination, the released heat produced from carbonaceous substrate during the combustion brings down the crystallization temperature required for the formation of nickel cobalt oxide spinel, and the evolution of large amounts of gasses (such as  $\text{CO}$ ,  $\text{CO}_2$  and water vapor) during the oxidative decomposition of carbonaceous substrate not only helps to disintegrate the large agglomerated particles with each other and form the porous structure, but also helps to inhibit the sintering of the nanosized particles, thus a finely divided, porous and small-size nanoparticles can be obtained especially at lower calcination temperature.

According to the above analysis, the differences of electrochemical performances of the  $\text{NiCo}_2\text{O}_4$  prepared by sol–gel method with different chelating agents can be attributed to the use of different chelating agents. The chelating agent molecules as a chelating ligand interact with metallic ions to form stable metal complex. During the calcination, due to the difference of the combustion heat generated from the decomposition of chelating agents, the crystallization temperature for the formation of  $\text{NiCo}_2\text{O}_4$  crystal will be different, thus leading to the differences in the size, pore structure and specific surface area for the obtained

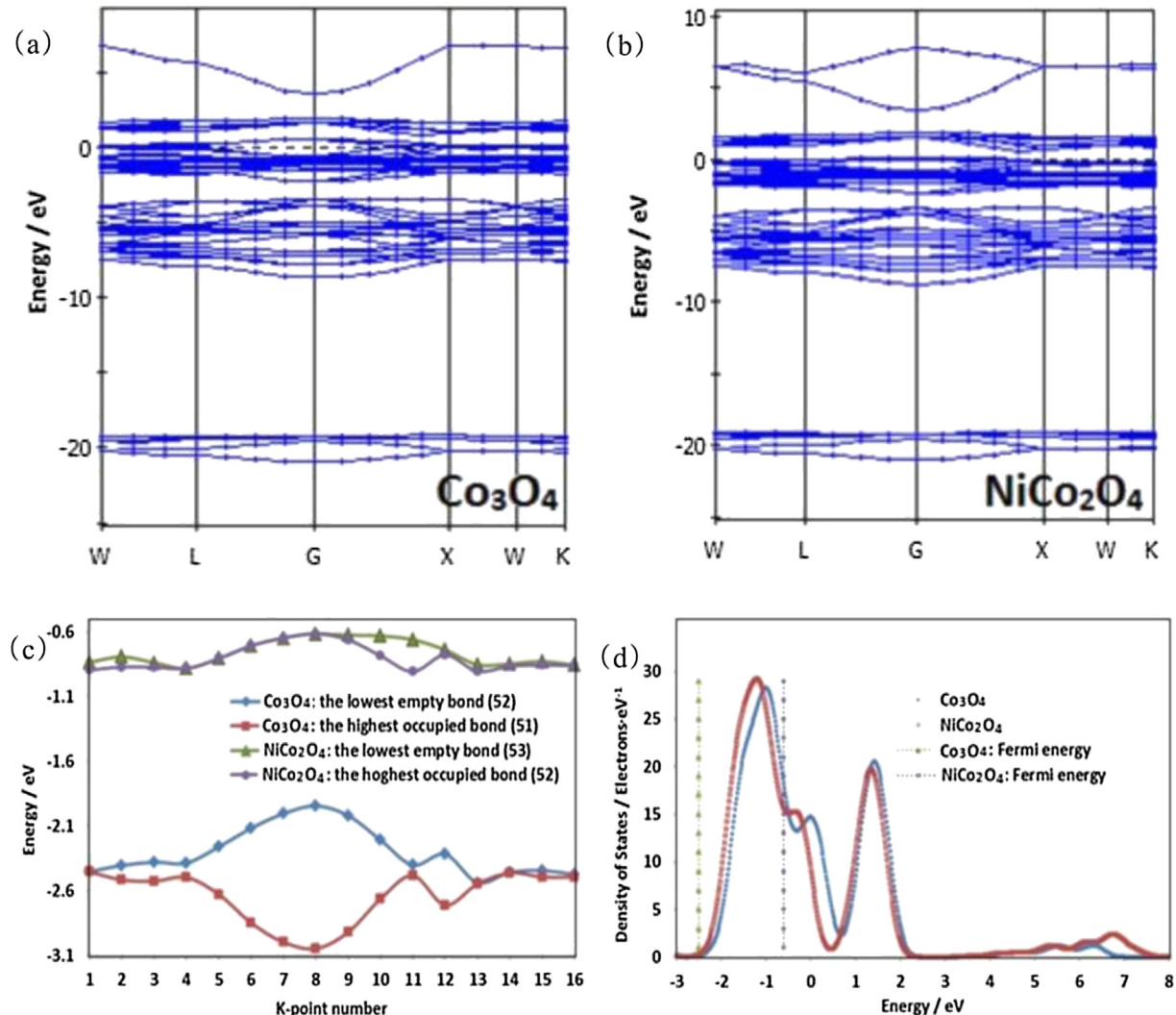


Fig. 7. Total band structures of  $\text{Co}_3\text{O}_4$  (a) and  $\text{NiCo}_2\text{O}_4$  (b). Comparison of frontier band structures of  $\text{Co}_3\text{O}_4$  and  $\text{NiCo}_2\text{O}_4$  (c). Comparison of density of states of  $\text{Co}_3\text{O}_4$  and  $\text{NiCo}_2\text{O}_4$  (d).

nano-particles. To summarize, different chelating agents used in the sol–gel method have great influences upon the particle size, pore structure and specific surface area of the spinel  $\text{NiCo}_2\text{O}_4$ , resulting in the differences of electrochemical properties as analyzed above.

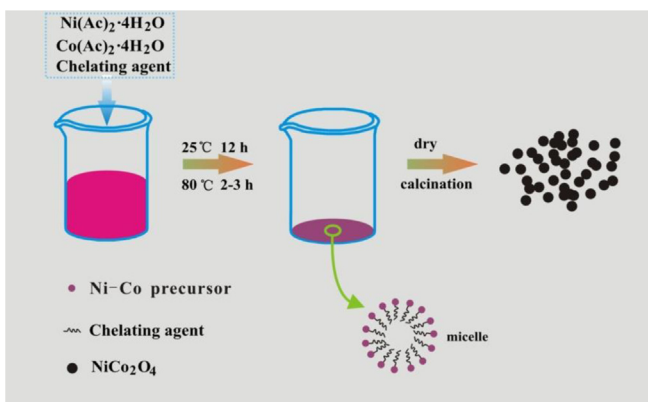


Fig. 8. Synthesis scheme for spinel  $\text{NiCo}_2\text{O}_4$ .

As demonstrated in Table 4, the specific capacitances of  $\text{NiCo}_2\text{O}_4$  of our present work and other studies are compared. Hu et al. [22] first obtained the  $\text{NiCo}_2\text{O}_4$  prepared by an epoxide-driven sol–gel process, and its specific capacitance reached an ultrahigh value of  $1400 \text{ F g}^{-1}$  ( $0.4 \text{ mg cm}^{-2}$  loading). More recently, Hu et al. [56] developed a simple and scalable process for synthesizing  $\text{NiCo}_2\text{O}_4$  nanocrystals through a thermal decomposition method, which demonstrated a high specific capacitance of  $764 \text{ F g}^{-1}$  ( $0.5 \text{ mg cm}^{-2}$  loading) at a scan rate of  $2 \text{ mV s}^{-1}$ . Lou et al. [40] successfully grew single-crystalline nanoneedle arrays of  $\text{NiCo}_2\text{O}_4$  through a simple solution together with a post annealing treatment, and it exhibited a high specific capacitance of  $1118.6 \text{ F g}^{-1}$  at a current density of  $5.56 \text{ mA cm}^{-2}$ . The  $\text{NiCo}_2\text{O}_4$  nanotubes were prepared by a single-spinneret electrospinning technique followed by calcination in air reported by Li et al. in the literature [43] and the obtained nanotubes manifested a high specific capacitance of  $1647 \text{ F g}^{-1}$  at a current density of  $1 \text{ A g}^{-1}$ . Ma et al. [28] obtained a maximum specific capacitance of  $671 \text{ F g}^{-1}$  for  $\text{NiCo}_2\text{O}_4$  nanoparticles synthesized by coprecipitation method at a current density of  $1 \text{ A g}^{-1}$  at  $0.6 \text{ mg cm}^{-2}$  loading mass. Yuan et al. [57] reported polymer-assisted synthesis of network-like  $\text{NiCo}_2\text{O}_4$  framework that demonstrated a specific capacitance of  $587 \text{ F g}^{-1}$  at a current

**Table 4**

Specific capacitance of the  $\text{NiCo}_2\text{O}_4$  prepared in present work and other reports in previous works. Some information such as preparation method and the mass loading of active material is included for better comparison among the different samples.

Sample	Specific capacitance	Preparation method	Mass loading of active material	Reference
$\text{NiCo}_2\text{O}_4$ aerogels	$1400 \text{ F g}^{-1}$ at a scan rate of $25 \text{ mV s}^{-1}$	Epoxide-driven sol–gel method	$0.4 \text{ mg cm}^{-2}$	22
$\text{NiCo}_2\text{O}_4$ nanocrystals	$764 \text{ F g}^{-1}$ at a scan rate of $2 \text{ mV s}^{-1}$	Thermal decomposition method	$0.5 \text{ mg cm}^{-2}$	56
$\text{NiCo}_2\text{O}_4$ nanowires	$1118.6 \text{ F g}^{-1}$ at a current density of $5.56 \text{ mA cm}^{-2}$	Solution method	/	40
$\text{NiCo}_2\text{O}_4$ nanotubes	$1647 \text{ F g}^{-1}$ at a current density of $1 \text{ A g}^{-1}$	Electrospinning method	/	41
$\text{NiCo}_2\text{O}_4$ nanoparticles	$671 \text{ F g}^{-1}$ at a current density of $1 \text{ A g}^{-1}$	Coprecipitation method	$0.6 \text{ mg cm}^{-2}$	28
$\text{NiCo}_2\text{O}_4$ powders	$587 \text{ F g}^{-1}$ at a current density of $2 \text{ A g}^{-1}$	Polymer-assisted solution method	$5 \text{ mg cm}^{-2}$	57
$\text{NiCo}_2\text{O}_4$ nanocrystals	$580 \text{ F g}^{-1}$ at a current density of $0.5 \text{ A g}^{-1}$	Electrochemical deposition	/	30
$\text{NiCo}_2\text{O}_4$ crystals	$217 \text{ F g}^{-1}$ at a current density of $1 \text{ mA cm}^{-2}$	Sol–gel method	$5.6 \text{ mg cm}^{-2}$	27
$\text{NiCo}_2\text{O}_4$ nanowires	$1284 \text{ F g}^{-1}$ at a current density of $2 \text{ A g}^{-1}$	Hydrothermal method	/	29
$\text{NiCo}_2\text{O}_4$ nanoparticles	$678 \text{ F g}^{-1}$ at a current density of $2 \text{ A g}^{-1}$	Citric acid assisted sol–gel method	$1 \text{ mg cm}^{-2}$	Present work
$\text{NiCo}_2\text{O}_4$ nanoparticles	$1254 \text{ F g}^{-1}$ at a current density of $2 \text{ A g}^{-1}$	Oxalic acid assisted sol–gel method	$1 \text{ mg cm}^{-2}$	Present work
$\text{NiCo}_2\text{O}_4$ nanoparticles	$576 \text{ F g}^{-1}$ at a current density of $2 \text{ A g}^{-1}$	EDTA assisted sol–gel method	$1 \text{ mg cm}^{-2}$	Present work

density of  $2 \text{ A g}^{-1}$  at  $5 \text{ mg cm}^{-2}$  loading mass. Gupta et al. [30] explored electrochemically synthesized nanostructured  $\text{NiCo}_2\text{O}_4$  thin film, which showed a specific capacitance of  $580 \text{ F g}^{-1}$  at a current density of  $0.5 \text{ A g}^{-1}$ . Wu et al. [27] reported the sol–gel synthesis of  $\text{NiCo}_2\text{O}_4$  crystals, and the specific capacitance of submicron-sized  $\text{NiCo}_2\text{O}_4$  crystals reached as much as  $217 \text{ F g}^{-1}$  at a current density of  $1 \text{ mA cm}^{-2}$  at a high mass loading of  $5.6 \text{ mg cm}^{-2}$ . Hu et al. [29] obtained the high specific capacitance of  $1284 \text{ F g}^{-1}$  for  $\text{NiCo}_2\text{O}_4$  nanowires prepared by hydrothermal method at a current density of  $2 \text{ A g}^{-1}$ . In our present work, the  $\text{NiCo}_2\text{O}_4$  were synthesized by CA, OA and EDTA assisted sol–gel method, and they respectively displayed a maximum specific capacitance of  $678$ ,  $1254$  and  $576 \text{ F g}^{-1}$  at a current density of  $2 \text{ A g}^{-1}$  at  $1 \text{ mg cm}^{-2}$  loading mass, which revealed its promising application in supercapacitors. From these results described above, we can conclude that the preparation methods have great impact on the physical and electrochemical properties of  $\text{NiCo}_2\text{O}_4$ . The chelating agent assisted sol–gel method is especially suitable for the preparation of high specific surface  $\text{NiCo}_2\text{O}_4$  as excellent supercapacitor electrode materials due to the high purity of the products, low-temperature synthesis, and easy realization of scalable production, which further demonstrates its potential with low cost for a replaced candidate of  $\text{RuO}_2$  in the application of supercapacitor as reported by Hu et al. [22].

#### 4. Conclusions

In summary, spinel  $\text{NiCo}_2\text{O}_4$  nanoparticles were successfully synthesized by a simple and scalable CA, OA and EDTA assisted sol–gel method. The chelating agent is a particularly important factor that affects the size of particles, pore structure and specific surface area of the  $\text{NiCo}_2\text{O}_4$ , thereby leading to the differences of their electrochemical properties; such observations are of fundamental importance allowing the tailoring of electrochemical properties through careful choice of chelating agent. The electrochemical characterizations reveal that the  $\text{NiCo}_2\text{O}_4$  prepared by OA displays the highest specific capacitance of  $1254 \text{ F g}^{-1}$  under a mass loading of  $1 \text{ mg cm}^{-2}$  at a current density of  $2 \text{ A g}^{-1}$ , and the  $\text{NiCo}_2\text{O}_4$  prepared by EDTA manifests the best rate capability and cycling stability. Furthermore, the first-principles calculations were used to investigate the electronic structure of  $\text{NiCo}_2\text{O}_4$ , which can explain the low observed resistance of the  $\text{NiCo}_2\text{O}_4$  which can be obtained from the EIS data, and hence help to further understand its excellent electrochemical behavior. Therefore, the good electrochemical properties coupled with the facile and cost-effective preparation method will render it attractive for promising application in supercapacitors.

#### Acknowledgments

The work is financially supported by the National Natural Science Foundation of China (51134007, 21003161 and 21250110060), the Distinguished Young Scientists of Hunan Province (13JJ1004), the Program for the New Century Excellent Talents in University (NCET-11-0513), and the Hunan Provincial Innovation Foundation for Postgraduate (CX2013B048).

#### References

- [1] G. Wang, L. Zhang, J. Zhang, *Chem. Soc. Rev.* 41 (2012) 797–828.
- [2] I. Hadjipaschalos, A. Poullikkas, V. Efthimiou, *Renew. Sustain. Energy Rev.* 13 (2009) 1513–1522.
- [3] J.R. Miller, P. Simon, *Science* 321 (2008) 651–652.
- [4] S.W. Lee, B.M. Gallant, H.R. Byon, P.T. Hammond, Y. Shao-Horn, *Energy Environ. Sci.* 4 (2011) 1972–1985.
- [5] F. Zhang, T. Zhang, X. Yang, L. Zhang, K. Leng, Y. Huang, Y. Chen, *Energy Environ. Sci.* 6 (2013) 1623–1632.
- [6] C.-Z. Yuan, B. Gao, X.-G. Zhang, *J. Power Sources* 173 (2007) 606–612.
- [7] W. Wei, X. Cui, W. Chen, D.G. Ivey, *Chem. Soc. Rev.* 40 (2011) 1697–1721.
- [8] Y. Zhai, Y. Dou, D. Zhao, P.F. Fulvio, R.T. Mayes, S. Dai, *Adv. Mater.* 23 (2011) 4828–4850.
- [9] A. Davies, A. Yu, *Can. J. Chem. Eng.* 89 (2011) 1342–1357.
- [10] J. Zhang, X.S. Zhao, *J. Phys. Chem. C* 116 (2012) 5420–5426.
- [11] K. Lota, V. Khomenko, E. Frackowiak, *J. Phys. Chem. Solids* 65 (2004) 295–301.
- [12] J.P. Zheng, P.J. Cygan, T.R. Jow, *J. Electrochem. Soc.* 142 (1995) 2699–2703.
- [13] M. Wu, J. Gao, S. Zhang, A. Chen, *J. Power Sources* 159 (2006) 365–369.
- [14] M. Nakayama, T. Kanaya, R. Inoue, *Electrochim. Commun.* 9 (2007) 1154–1158.
- [15] L. Mayrand-Provencher, D. Rochelefort, *J. Phys. Chem. C* 113 (2009) 1632–1639.
- [16] C. Yuan, X. Zhang, L. Su, B. Gao, L. Shen, *J. Mater. Chem.* 19 (2009) 5772–5777.
- [17] X. Wang, Y. Li, *J. Am. Chem. Soc.* 124 (2002) 2880–2881.
- [18] S.K. Meher, G.R. Rao, *J. Phys. Chem. C* 115 (2011) 15646–15654.
- [19] V. Srinivasan, J.W. Weidner, *J. Power Sources* 108 (2002) 15–20.
- [20] C.-C. Hu, W.-C. Chen, *Electrochim. Acta* 49 (2004) 3469–3477.
- [21] Y. Zhu, X. Ji, C. Pan, Q. Sun, W. Song, L. Fang, Q. Chen, C.E. Banks, *Energy Environ. Sci.* 6 (2013) 3665–3675.
- [22] T.-Y. Wei, C.-H. Chen, H.-C. Chien, S.-Y. Lu, C.-C. Hu, *Adv. Mater.* 22 (2010) 347–351.
- [23] S. Verma, H.M. Joshi, T. Jagadale, A. Chawla, R. Chandra, S. Ogale, *J. Phys. Chem. C* 112 (2008) 15106–15112.
- [24] B. Cui, H. Lin, J.-B. Li, X. Li, J. Yang, J. Tao, *Adv. Funct. Mater.* 18 (2008) 1440–1447.
- [25] Y.E. Roginskaya, O.V. Morozova, E.N. Lubnin, Y.E. Ulitina, G.V. Lopukhova, S. Trasatti, *Langmuir* 13 (1997) 4621–4627.
- [26] R. Alcántara, M. Jaraba, P. Lavela, J.L. Tirado, *Chem. Mater.* 14 (2002) 2847–2848.
- [27] Y.Q. Wu, X.Y. Chen, P.T. Ji, Q.Q. Zhou, *Electrochim. Acta* 56 (2011) 7517–7522.
- [28] C. Wang, X. Zhang, D. Zhang, C. Yao, Y. Ma, *Electrochim. Acta* 63 (2012) 220–227.
- [29] R. Zou, K. Xu, T. Wang, G. He, Q. Liu, X. Liu, Z. Zhang, J. Hu, *J. Mater. Chem. A* 1 (2013) 8560–8566.
- [30] V. Gupta, S. Gupta, N. Miura, *J. Power Sources* 195 (2010) 3757–3760.
- [31] J. Sun, Y. Zhang, W. Fan, D. Wu, Y. Sun, *Prog. Chem.* 11 (1999) 80–85.
- [32] J. Liu, Y. Zhou, C. Liu, J. Wang, Y. Pan, D. Xue, *CrystEngComm* 14 (2012) 2669–2674.
- [33] P.D. Battle, A.K. Cheetham, J.B. Goodenough, *Mater. Res. Bull.* 14 (1979) 1013–1024.
- [34] M.S.G. Baythoun, F.R. Sale, *J. Mater. Sci.* 17 (1982) 2757–2769.

[35] B. Lefez, P. Nkeng, J. Lopitaux, G. Poillerat, *Mater. Res. Bull.* 31 (1996) 1263–1267.

[36] N. Chaubal, V. Joshi, *J. Porous Mater.* 18 (2011) 177–183.

[37] M.-C. Liu, L.-B. Kong, C. Lu, X.-M. Li, Y.-C. Luo, L. Kang, *ACS Appl. Mater. Interfaces* 4 (2012) 4631–4636.

[38] S.K. Meher, P. Justin, G. Ranga Rao, *ACS Appl. Mater. Interfaces* 3 (2011) 2063–2073.

[39] R.N. Singh, J.F. Koenig, G. Poillerat, P. Chartier, *J. Electrochem. Soc.* 137 (1990) 1408–1413.

[40] G.Q. Zhang, H.B. Wu, H.E. Hoster, M.B. Chan-Park, X.W. Lou, *Energy Environ. Sci.* 5 (2012) 9453–9456.

[41] J.W. Lee, A.S. Hall, J.-D. Kim, T.E. Mallouk, *Chem. Mater.* 24 (2012) 1158–1164.

[42] M.D. Stoller, R.S. Ruoff, *Energy Environ. Sci.* 3 (2010) 1294–1301.

[43] L. Li, S. Peng, Y. Cheah, P. Teh, J. Wang, G. Wee, Y. Ko, C. Wong, M. Srinivasan, *Chem. Eur. J.* 19 (2013) 5892–5898.

[44] C.C. Hu, C.-T. Hsu, K.-H. Chang, H.-Y. Hsu, *J. Power Sources* 238 (2013) 180–189.

[45] H.-Y. Hsu, K.-H. Chang, R.R. Salunkhe, C.-T. Hsu, C.C. Hu, *Electrochim. Acta* 94 (2013) 104–112.

[46] Z. Fan, J. Yan, T. Wei, L. Zhi, G. Ning, T. Li, F. Wei, *Adv. Funct. Mater.* 21 (2011) 2366–2375.

[47] R.B. Rakhi, W. Chen, D. Cha, H.N. Alshareef, *J. Mater. Chem.* 21 (2011) 16197–16204.

[48] M.D. Stoller, S. Park, Y. Zhu, J. An, R.S. Ruoff, *Nano Lett.* 8 (2008) 3498–3502.

[49] Y. Li, P. Hasin, Y. Wu, *Adv. Mater.* 22 (2010) 1926–1929.

[50] Z.T. Yang Siqi, Zhanliang Tao, Jun Chen, *Acta Chim. Sin.* 71 (2013) 1029–1034.

[51] U. Mizutani, *Introduction to the Electron Theory of Metals*, Cambridge University Press, United Kingdom, 2001.

[52] J. Liu, C. Liu, Y. Wan, W. Liu, Z. Ma, S. Ji, J. Wang, Y. Zhou, P. Hodgson, Y. Li, *CrystEngComm* 15 (2013) 1578–1585.

[53] A. Saberi, F. Golestanian-Fard, H. Sarpoolaky, M. Willert-Porada, T. Gerdes, R. Simon, *J. Alloys Compd.* 462 (2008) 142–146.

[54] A.B. Panda, A. Pathak, P. Pramanik, *Mater. Lett.* 52 (2002) 180–186.

[55] G.T.-K. Fey, Y.-D. Cho, T. Prem Kumar, *Mater. Chem. Phys.* 87 (2004) 275–284.

[56] C.-T. Hsu, C.-C. Hu, *J. Power Sources* 242 (2013) 662–671.

[57] C. Yuan, J. Li, L. Hou, J. Lin, X. Zhang, S. Xiong, J. Mater. Chem. A 1 (2011) 11145–11151.